applied optics

Coherent superresolution imaging via grating-based illumination

Jeffrey P. Wilde,[1,*] Joseph W. Goodman,[1] Yonina C. Eldar,[2] and Yuzuru Takashima[3]

[1]Department of Electrical Engineering, Stanford University, Stanford, California 94305, USA
[2]Department of Electrical Engineering, Technion, Haifa 32000, Israel
[3]College of Optical Sciences, The University of Arizona, Tucson, Arizona 85721, USA
*Corresponding author: jpwilde@stanford.edu

Received 20 July 2016; revised 17 October 2016; accepted 17 October 2016; posted 18 October 2016 (Doc. ID 270944); published 17 November 2016

This paper describes two superresolution coherent imaging techniques, which both use a diffraction grating to direct high spatial frequency information that would otherwise be lost through the imaging system pupil. The techniques employ digital holography to measure the optical field in the image plane and rely on capturing multiple holograms with the illumination condition altered between exposures. In one case, we used linear signal processing to separate aliased spectral regions, while in the second case we directly measured spectral regions without aliasing. In both cases, we stitched together higher-bandwidth synthetic aperture spectra and used them to reconstruct superresolution images. Our experimental results validated the approaches, demonstrating a resolution gain factor of approximately 2.5.

OCIS codes: (100.6640) Superresolution; (110.1758) Computational imaging; (110.3010) Image reconstruction techniques.

http://dx.doi.org/10.1364/AO.56.000A79

1. INTRODUCTION

A variety of approaches have been previously investigated to provide improved resolution of optical imaging systems beyond the classical diffraction limit as determined by the numerical aperture (NA) and wavelength (λ), although such approaches are typically constrained by a resolution limit of $\lambda/2n$, where n is the refractive index in image space [1,2]. This excludes near-field imaging, super-resolved fluorescence microscopy (Ref. [2], Section 18.2), and imaging of sparse objects using compressed sensing techniques [3]. Resolution enhancement allows one to use a low-NA objective lens having a long working distance and large field of view, while simultaneously obtaining resolution comparable to a higher NA system. Schemes to accomplish this task fall under the general classification of superresolution imaging.

The potential of superresolution was recognized early on by Adolf Lohmann and his co-workers. In 1964, for example, Lohmann and Paris described an approach to double the resolution of an imaging system using two orthogonal polarization states to illuminate a non-birefringent object from two different angles [4]. Indeed Lohmann and his colleagues continued to make pioneering advancements in this field over many decades, including the development of the idea that superresolution can be viewed in the Wigner domain as a manipulation of an optical system's degrees of freedom [5,6]. A common example includes trading temporal bandwidth for improved spatial resolution, which is the approach adopted in this paper.

Additional early work on superresolution, first reported by Lukosz in 1966 and subsequently extended by other researchers, involved the use of two static gratings, one near the object and the other near the image plane. However, this approach leads to ghost image formation that restricts the field of view [7,8] or dynamic range [9]. Alternatively, the two gratings can be synchronously moved and the detected image temporally averaged to eliminate spurious ghost images [10,11], but this configuration is more complicated to implement and has only been demonstrated with unity magnification. Additional techniques include structured illumination of fluorescent objects [12], as well as oblique illumination schemes over a restricted range of illumination angles [13,14]. It is also possible to construct a coherent imaging system with an oblique illumination beam that does not pass through the imaging pupil, but instead is either re-injected on the low-NA side of the objective lens at the proper location and with the correct phase in the Fourier plane [15] or is mixed with a second, lower-angle illumination beam that is allowed through the pupil [16].

Various coherent detection techniques based on digital holography have also been investigated to achieve superresolution. Off-axis digital holography has been combined with synthetic aperture formation to increase the resolution of a lensless

Fourier holography setup, but this approach required translating the detecting camera in two dimensions over several millimeters [17]. Liu *et al.* have reported a related approach in which the camera remained stationary and a grating was placed after the object to direct higher spatial frequency content to the hologram [18]. In this case, numerical reconstruction provided an image with improved resolution, although the effective NA was still quite low. Liu's grating-based technique has been extended using a two-dimensional (2D) dynamic phase grating that offers electro-optic control of the diffraction efficiency [19]. Hillman *et al.* proposed a different approach that involved a single oblique illumination angle combined with rotation of the sample and capture of several digital holograms [20].

In this paper, we present two approaches to implement coherent superresolution imaging [21–23]. They both use a grating element to direct high-frequency content from the object through the imaging aperture. To accomplish the desired extension of resolution, it is necessary to measure the *complex amplitude* of the field in the image plane. This measurement can be done via digital holography by bringing in a tilted reference wave, coherent with respect to the field in the image plane, to interfere with this field and thus create a hologram. Digitally filtering the hologram to eliminate all but one sideband, and then translating that sideband to be centered on zero frequency can recover the complex field in the image plane. The techniques reported here, which fall under the general heading of "synthetic aperture holography" (Ref. [2], Section 18.1.2), are fundamentally based on spatially coherent imaging and are therefore not applicable to fluorescent objects.

2. METHODS

The first approach, referred to as grating-based pupil multiplexing, uses a single grating that is either imaged onto the object or placed in near contact with the object to alias high-frequency content through the pupil. When in near contact, the grating is ideally placed in front of the object so that the diffracted orders provide a set of illumination waves, as shown in Fig. 1. If the grating follows the object, then only the non-evanescent portion of the object spectrum for normal incidence is considered. The grating produces copies of the object's angular spectrum that are shifted from one another by multiples of the grating frequency. The pupil low-pass filters this set of spectra. Within the pupil, the various shifted portions of the object spectrum combine linearly with coefficients nominally given by the Fourier series coefficients of the grating. Digital holography provides coherent detection of the optical field in the image plane. Data acquisition involves the capture of multiple holograms with the grating shifted by a fraction of its period between exposures. Linear signal processing is then used to de-alias the spectral regions and numerically reconstruct a complex-valued image with superresolution in one dimension.

This approach is analogous to an electronic modulated-wideband converter (MWC) designed to reduce the sampling rate in analog-to-digital conversion [24–26]. The MWC allows recovery of a high-bandwidth signal from the output of several low-passed versions of the signal, where the different branches correspond to modulations of the input by a periodic function. The pupil multiplexing scheme described here can be viewed as an optical version of the MWC in which a low-NA lens replaces the low-pass filter, a movable grating replaces the modulations, and digital signal processing is used to construct the final high-bandwidth output signal.

The second approach is based on oblique illumination by a number of individual collimated beams directed sequentially to the object over a set of off-axis incidence angles. It is possible to generate the various illumination angles by translating a normally incident collimated beam across a grating element, as shown in Fig. 2. In general, a specially constructed 2D tiled grating can be envisioned, each tile element producing a first-order diffracted beam directed at the object with a unique 2D angle. The collimated beam has a diameter that is slightly less than the linear dimension of a tile segment. In this case, the tiled grating structure is placed in front of the object, but not in near contact. Therefore, the illumination path is constructed with a specified working distance that separates the grating element from the object. A simpler 1D version of this method uses a uniform grating with multiple diffraction orders; the normally incident collimated beam is then translated to specific locations across the grating to direct individual diffraction orders to the object. As with the 1D pupil multiplexing scheme, the grating can be rotated and the process repeated to obtain 2D superresolution.

A notable feature of the two approaches is that they are straightforward to implement, with both being based on a single grating element to generate a wide synthetic aperture. By using diffraction gratings, these techniques can readily yield large plane-wave illumination angles without high-NA lenses in the illumination path. As with any coherent digital holographic imaging system, the resulting images yield quantitative phase information and offer the ability to implement numerical focusing.

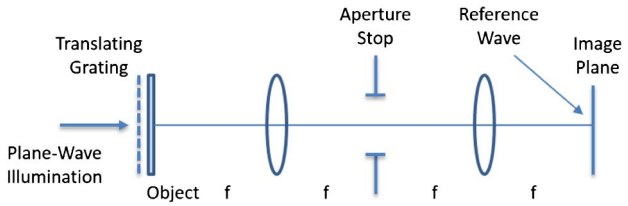

Fig. 1. Grating-based pupil multiplexing.

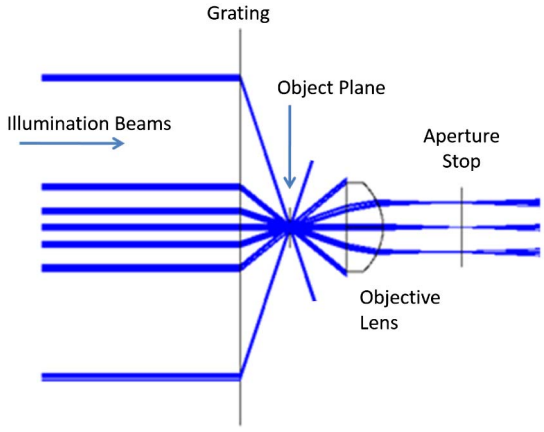

Fig. 2. Grating-based oblique illumination method.

3. THEORETICAL DESCRIPTION

A. Grating-Based Pupil Multiplexing

In this section, we limit the analysis to a 1D formulation, but the extension to two dimensions is straightforward. Consider a coherent imaging system and suppose that a high-frequency grating is placed in close proximity to the object being imaged, either just before the object or just after it. The grating amplitude transmittance is a periodic function with fundamental frequency f_g, which we represent by $P(x)$. This function can be expanded in a complex Fourier series,

$$P(x) = \sum_{n=-\infty}^{\infty} p_n \exp(-j2\pi n f_g x). \tag{1}$$

Furthermore, we assume that the grating has been fabricated such that it possesses a finite set of lower-order Fourier coefficients p_n that are approximately equal in magnitude, meaning that all the plane wave components illuminating the object are of approximately equal magnitude, while the remaining higher-order p_n are close to zero. For example, a Dammann phase grating provides such a response.

If $t_0(x)$ represents the complex amplitude transmittance of the object, which is the quantity we wish to recover, then the field leaving the sandwiched object and grating is given by

$$t_o(x)P(x) = t_o(x) \sum_{n=-\infty}^{\infty} p_n \exp(-j2\pi n f_g x). \tag{2}$$

The spectrum of $t_o(x)P(x)$, which is incident on the pupil plane, is then given by

$$U(\nu_x) = T_o(\nu_x) * \sum_{n=-\infty}^{\infty} p_n \delta(\nu_x - n f_g), \tag{3}$$

where $T_o(\nu_x)$ is the object spectrum and $*$ signifies convolution. We explicitly assume that the grating is located before the object. If the grating follows the object, then only the propagating portion of the object spectrum for normal incidence should be considered.

In the absence of the grating, the pupil of the imaging system restricts the light that passes through the aperture stop to a finite region of the spectrum. Consequently, important information about the object detail is lost. The effect of the grating is to multiplex different parts of the object spectrum into the pupil. Each diffraction order directs a specific spectral region, which we also refer to as a "spectral island," through the aperture stop. Assume that N diffraction orders are present. The resulting image will not resemble the object, but a high-resolution image can be recovered by acquiring a series of $K \geq N$ holograms, each taken with an appropriate change in the grating Fourier coefficients p_n. We show that it is then possible to separate the overlapping regions of the spectrum and stitch them back together in proper order, yielding a broader spectrum of the object (by a factor $<N$) than would otherwise pass the pupil.

We now briefly consider the digital processing performed on a set of $2K+1$ measured fields in the pupil (we use $2K+1$ measurements and $2N+1$ grating orders rather than K measurements and N orders for mathematical convenience). Continuing with a one-dimensional analysis, the kth detected image amplitude can be written as

$$A_k(\nu_x) = \sum_{n=-N}^{N} p_{k,n} T_o(\nu_x - n f_g) \mathrm{rect}(\nu_x / 2 f_p), \quad k = -K, \ldots K, \tag{4}$$

where the grating coefficients $p_{k,n}$ change for each of the $2K+1$ image captures, the rectangle function represents the finite pupil having a half-width frequency of f_p, and we assume that the grating frequency is chosen such that $f_g = \sigma f_p$, where σ is a factor between 0 and 1. In this way, the ± 1 diffraction components reside within the pupil, and the grating therefore produces aliasing with overlapping spectral regions. In practice, σ is taken to be between 0.75–0.90. For a circular pupil, the spectral overlap is necessary to avoid gaps in the enhanced spectrum and, when the grating coefficients p_n are not completely known, we can also use the overlap regions in signal processing as discussed in the next section.

Equation (4) can be rewritten in matrix-vector form as

$$\vec{A}(\nu_x) = \mathbf{P}\vec{T}(\nu_x), \tag{5}$$

where

$$\vec{A}(\nu_x) = \begin{bmatrix} A_{-K}(\nu_x) \\ \vdots \\ A_K(\nu_x) \end{bmatrix}, \tag{6}$$

and

$$\vec{T}(\nu_x) = \begin{bmatrix} T_o(\nu_x + N f_g)\mathrm{rect}(\nu_x/2f_p) \\ \vdots \\ T_o(\nu_x - N f_g)\mathrm{rect}(\nu_x/2f_p) \end{bmatrix}, \tag{7}$$

and $\mathbf{P}$ is a $(2K+1) \times (2N+1)$ matrix

$$\mathbf{P} = \begin{bmatrix} p_{-K,-N} & \cdots & p_{-K,N} \\ \vdots & \vdots & \vdots \\ p_{K,-N} & \cdots & p_{K,N} \end{bmatrix}. \tag{8}$$

Consider first the case in which $K = N$ so that $\mathbf{P}$ is square. If the grating constants are chosen such that the matrix $\mathbf{P}$ is non-singular and well conditioned, then $\mathbf{P}^{-1}$ exists and the spectral islands can be separated through

$$\vec{T}(\nu_x) = \mathbf{P}^{-1}\vec{A}(\nu_x). \tag{9}$$

A convenient choice for the grating coefficients $p_{k,n}$ corresponds to grating translation by $\Delta x = 1/[f_g(2K+1)]$ between image captures (i.e., to equal-increment steps spanning one period). Each such step changes the phase of the nth grating Fourier coefficient by $\Delta\phi_n = 2\pi n/(2K+1)$.

Once the individual spectral islands are known, they can be translated to their proper frequency positions and combined to synthesize a broader spectrum. Specifically, the image spectrum half-width increases from f_p to $(\sigma N + 1)f_p$, where $(\sigma N + 1)$ is the resolution gain factor. More detail associated with the stitching together of spectral regions is provided in Section 4. However, as mentioned previously, it generally requires some degree of overlap between adjacent regions, particularly when $\mathbf{P}$ is not entirely known, which can be the case in the presence of various experimental perturbations.

More than $2N + 1$ measurements can be made to improve the signal-to-noise ratio, with the result that the **P** matrix is no longer square but can still be readily (left-) inverted with a psuedoinverse operation. Because the imaging system is coherent, no OTF compensation is required, unlike the case of incoherent superresolution imaging with structured illumination [27].

B. Sequential Oblique Illumination

For the sequential oblique illumination method, the number of measurements equals the number of illumination angles. Aliasing is avoided, which improves the accuracy of the technique. The spectral islands are therefore individually measured and numerically stitched together to form the higher frequency composite spectrum.

4. DATA ANALYSIS

A primary benefit of grating illumination relates to the fact that the diffraction orders are separated uniformly in spatial frequency with high intrinsic angular precision, which in turn facilitates shifting of the spectral sections to their correct locations when reconstructing the enhanced image spectrum. In both the pupil-multiplexing and sequential synthetic aperture schemes, the zero-order and first-order beams are allowed to pass through the pupil, and their positions in frequency space are directly measured. If the imaging system is aplanatic (which is not particularly difficult to achieve, especially at low NA), then a linear relationship exists between the locations of the diffraction orders in frequency space. In other words, even though the higher-order beams are blocked at the pupil, the proper positions for the higher-order spectral islands can be very easily determined with high accuracy from knowledge of the zero- and first-order positions. Other non-grating-based methods to generate a set of illumination angles may not provide a similar intrinsic benefit and could therefore add additional complexity to the optical setup and/or the data analysis. In the remainder of this section, we focus on the signal processing details associated with constructing a **P** matrix applicable to an experimental setup with grating illumination in which a number of factors must be considered.

First consider pupil multiplexing based on equal-increment grating steps, with the number of steps equal to the number of diffraction orders. The ideal **P** is square and takes on a simple form with matrix elements given by

$$p_{k,n} = \exp[-j2\pi kn/(2N+1)], \qquad k, n = -N, \ldots N. \quad \textbf{(10)}$$

This matrix is unitary with an inverse equal to its conjugate transpose. In practice, however, there can be errors in the grating position during stepping, as well as an uncertainty of the grating's initial location. There may also be a small phase drift of the interferometer in between exposures, and the optical system might, for various reasons, impart different phase shifts to otherwise symmetric diffraction orders. In the next section, for example, we show an experimental setup that uses a spatial filter to equalize the powers of the diffraction orders, but this filter also imparts unequal relative phase shifts to the various orders. All of these effects conspire to perturb the ideal **P** matrix to a version denoted by $\widetilde{\mathbf{P}}$ as

$$\widetilde{p}_{k,n} = \frac{A_n}{A_0} \exp\left\{-j\left[\frac{2\pi kn}{2K+1} + \theta_k + \delta_{k,n} + \phi_n\right]\right\}, \quad k = -K, \ldots K; n = -N, \ldots N. \quad \textbf{(11)}$$

Here A_n is the real-valued amplitude of the nth-order beam, θ_k is the interferometer phase drift between exposures, $\delta_{k,n}$ is the phase error of the nth diffraction order (relative to the zero-order) due to a grating position error in the kth step, and ϕ_n accounts for phase shifts of the non-zero orders (again relative to the zero-order) associated with an arbitrary starting position for the grating as well as any order-dependent phase error associated with propagation through the optical system. We note that $\phi_0 = 0$ and $\delta_{k,0} = 0$ because the zero-order phase, relative to the reference beam, is already fully captured by inclusion of the θ_k term. In addition, from the basic properties of a grating, we know that $\delta_{k,n} = n\delta_{k,1}$, where $\delta_{k,1}$ is the phase of the $+1$ order relative to the zero-order.

Fortunately, the following approach can accommodate the extra terms in Eq. (11). First, the imaging system is constructed so that the ±1 order beams are allowed to pass through the edge of the pupil, with these orders typically located at 75%–90% of cutoff. We then assume that the object spectrum near the edge of the pupil is weak compared to the magnitude of the ±1 diffracted orders, so the complex amplitudes of the zero- and first-order beams can be approximated by the corresponding directly measured spectral peaks. A similar approach has been used in structured illumination to estimate the phase of the sinusoidal illumination pattern ([28], Eq. 16). In our case, the imaging system is coherent, so the ±1 peaks are not attenuated by the transfer function as occurs for incoherent imaging. Thus, for each of the k grating steps, the measured complex amplitudes of the three spectral peaks are simply extracted from the corresponding measured hologram spectrum and set equal to the values of $\widetilde{p}_{k,n}$ (for $n = -1$, 0, and $+1$). The magnitudes of the first-order components (A_{-1} and A_{+1}) are normalized by A_0.

The next task is to determine the remaining higher-order components of the $\widetilde{\mathbf{P}}$ matrix. In this regard we note that the measured matrix elements comprising the central three columns of $\widetilde{\mathbf{P}}$ can be used to obtain some of the individual phase terms in Eq. (11). Most obvious are the interferometer phase drift terms θ_k, which are taken directly from the centermost $n = 0$ column. Any phase drift of the 0-order beam relative to the reference beam that occurs between grating steps will appear as a change in the complex amplitude of the central spectral peak ($n = 0$). The same phase drift θ_k will apply to all diffraction orders for the kth step. By subtracting θ_k from the measured phases of the $n = -1$ and $n = +1$ columns, we are left with the three remaining phase terms in Eq. (11). At this point, to visualize the impact of the three separate terms, it is helpful to plot the measured phase for the $n = \pm 1$ matrix elements (minus interferometer drift) as a function of k. For purposes of illustration, Fig. 3 shows such a plot with $K = 5$ for both the ideal case described by Eq. (10), as well as a more realistic simulated case that includes random grating position errors $\delta_{k,n}$ and order-dependent phase offsets ϕ_n. The line for the $n = -1$ terms has a slope equal in magnitude but opposite in sign to that for the $n = +1$ terms. Grating position

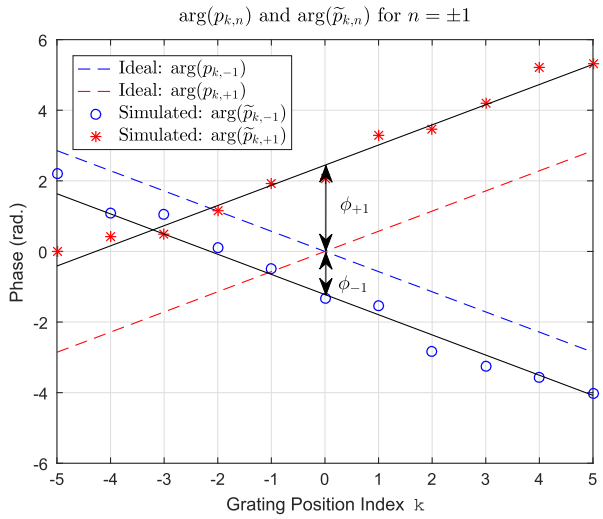

Fig. 3. Plots of the $n = \pm 1$ matrix-element phases for the ideal pupil multiplexing case of Eq. (10), along with a more realistic simulated case based on Eq. (11) after subtracting out the interferometer phase drift terms θ_k. Values for ϕ_{-1} and ϕ_{+1} are identified as vertical shifts from the ideal case.

noise causes the data points to deviate slightly from a perfect line. In Fig. 3, the noise is exaggerated to demonstrate the point by assuming a Gaussian distribution with a standard deviation of 0.25 radians. With modern nano-positioning hardware this error should be quite small. Going forward, we assume that the $\delta_{k,n}$ terms are negligible.

Figure 3 shows that the values for ϕ_{-1} and ϕ_{+1} can be found by noting how far the two solid lines are shifted vertically relative to the ideal situation. If $\phi_{-1} = -\phi_{+1}$, then the phase offset can be attributed solely to a grating position offset; otherwise, some other aspect of the optical system is contributing to a phase imbalance between the two first-order beams. In the former case, the impact of the grating position offset can be easily extrapolated to find the higher-order ϕ_n terms. However, in the latter instance, which is the more general situation, it may be impossible to know how the higher-order beams are affected by the optical path, so the first-order data are not adequate to estimate the higher-order matrix elements of $\widetilde{\mathbf{P}}$ (i.e., elements having $|n| \geq 2$).

To deal with the general case, we used the fact that in frequency space the spectral islands overlap with one another, and employed an optimization scheme to find values for the higher-order matrix elements that yielded the best self-consistency in the overlap regions. For example, take the case of $N = K = 2$, which corresponds to a 5×5 $\widetilde{\mathbf{P}}$ matrix. The central three columns of $\widetilde{\mathbf{P}}$ were directly measured. The interferometer phase drift terms θ_k were extracted from the $n = 0$ middle column. We generated the initial values for the two outermost columns ($n = \pm 2$) by taking the ideal matrix elements and adding the measured interferometer phase drifts. We assumed the grating position error phase terms $\delta_{k,n}$ to be negligible (although in general their values for $n = \pm 1$ could be extracted from the measurements, as illustrated in Fig. 3, and then used to determine the higher-order values). The phase offset terms ϕ_{-2} and ϕ_{+2} were taken as free parameters and scanned in discrete steps over 2π. This yielded a sequence of trial $\widetilde{\mathbf{P}}$ matrices, and our goal was to determine which member of the sequence yielded the best result in terms of spectral self-consistency. For each step in the sequence, we computed $\widetilde{\mathbf{P}}^{-1}$ and then found the corresponding spectral islands and shifted them to their proper center locations. Throughout the overlap regions of the ± 1 and ± 2 spectral islands, we compared the values of the spectra, which are 2D arrays of complex numbers, on a pixel-by-pixel basis using an objective function equal to the sum of the squared magnitude of the pixel differences. The best match, and hence the best self-consistency, occurred when ϕ_{-2} and ϕ_{+2} took on values that minimized the objective function. (The $\phi_{\pm 2}$ terms can actually be found independently of one another by optimizing the local spectral overlap associated with each term by itself, meaning these two phase terms can be found by two 1D optimizations as opposed to one 2D optimization.) A similar technique can be used to find the optimum magnitudes A_{-2} and A_{+2} by modifying the objective function to become the sum of the pixel intensity differences. We have now constructed the full 5×5 $\widetilde{\mathbf{P}}$ matrix that accounts for system perturbations and phase offsets, and is applicable to the measured data. This approach can likely be extended to deal with even higher orders (e.g., $n = \pm 3, \pm 4$), although we have not investigated this possibility in detail.

For sequential oblique illumination, we directly measured the individual spectral islands without aliasing. In this case, one can simply ignore weak higher-order illumination components (by simply not using them); however, in contrast, with pupil multiplexing it is important to include all diffraction orders with non-negligible power in the $\widetilde{\mathbf{P}}$ matrix. Construction of the composite superresolution spectrum can be accomplished in a similar manner as described above for pupil multiplexing; namely the process begins with the central three islands, and the composite spectrum is stitched together by progressively working outward to higher spatial frequencies, incrementally attaching spectral islands that have each been multiplied by a complex scale factor to make them consistent with their lower frequency neighbors.

5. EXPERIMENTAL RESULTS

A. Grating-Based Pupil Multiplexing

We constructed an experimental pupil multiplexing test system with 1D resolution enhancement, illustrated in Fig. 4, to demonstrate the technique. A He–Ne laser served as a coherent source, and we split the beam to form a Mach–Zehnder interferometer, with the imaging system placed in one arm. The imaging path comprised a 20-mm focal length objective lens (Thorlabs AC080-20) combined with a 200-mm focal length tube lens (Thorlabs LA1708), yielding 10X magnification. We used a CMOS camera (Thorlabs DCC1545M, 1280×1024 pixels, 5.2 um × 5.2 um pixel size) for off-axis digital holographic detection.

For simplicity, we used a Ronchi ruling (Edmund Optics 56-602, 2500 lp/inch) as the grating in this initial work. Because such a grating has multiple diffraction orders with varying strengths, we implemented front-end illumination optics to limit the number of transmitted orders and to balance

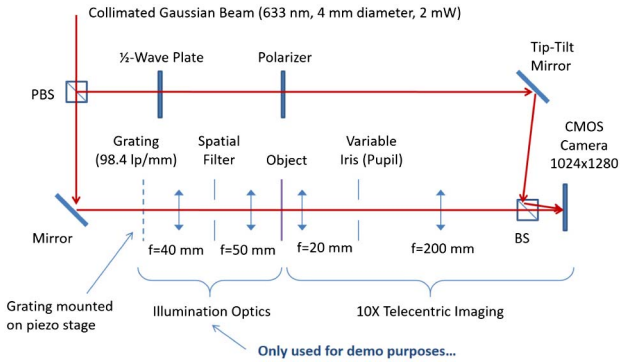

Fig. 4. Pupil multiplexing experimental demonstration setup.

their powers via spatial filtering. The underlying technique, though, will ultimately not rely on such illumination optics. A piezo-electric actuator (Physik Instrumente P-713 XY stage with E-662 controller) moved the grating in a sequence of equal-increment steps across one period. A digital hologram was captured at each step. The sequence of holograms was post-processed as described in Sections 3 and 4 to yield a much broader image spectrum. Using a Ronchi grating of 98.4 lp/mm (2500 lp/inch) with an illumination system magnification of 1.25 yielded an effective grating illumination frequency of 78.7 lp/mm. We used a variable aperture iris to control the imaging pupil size. A spatial filter mask in the illumination path restricted the highest orders to ± 2 and also approximately equalized the powers of the diffracted beams.

Figure 5(a) shows the object, which was a standard USAF test target acquired with the pupil wide open (NA ~ 0.18). For subsequent experimental testing, we reduced the pupil diameter to yield a coherent imaging passband cutoff frequency of approximately 100 lp/mm ($NA_0 = 0.063$). In this way, the ± 1 orders were able to pass through the imaging system ($\sigma = 0.79$), but higher orders were cut off. Five image hologram exposures were then recorded while stepping the grating in five equal-increment steps (2.03 μm/step). We zero-padded each digital hologram to become a 2048×2048 array and applied a 2D FFT. Figure 5(b) shows an example of one such hologram spectrum. We readily identified the complex field within the imaging system pupil and extracted it for subsequent analysis. Linear signal processing as described in the previous section yielded five de-aliased spectral islands.

Figure 6 shows our experimental results. The left column shows the magnitude of image spectra plotted on a log scale (spanning six orders of magnitude) with progressively increasing horizontal resolution, and the right column displays the associated intensity images. These images correspond to a small region of the test target as indicated by the inset box in Fig. 5(a), which contains the smallest set of features available on the target (Group 7, Elements 3-6). We found the images, which are plotted on a linear scale, by inverse Fourier transforming the spectra after zero padding to restore spatial sampling equivalent to the camera pixel dimensions. The first pair of results in the upper row of Figs. 6(a) and 6(b) are for the baseline imaging system with no resolution enhancement ($NA_0 = 0.063$). The results show that no bar patterns were resolved. The second row shows the case when the center three spectral islands (0 and ± 1 orders) were combined, so that two of the vertical bar patterns, Elements 3 and 4, were resolved. The resolution gain factor was 1.8 (i.e., $NA_1 = 0.114$), and the observed new cutoff frequency of 181 lp/mm (Group 7, Element 4) agreed very well with the expected theoretical value of $NA_1/\lambda = 180$ lp/mm. Finally, the bottom row shows the results using all five spectral islands. For this case, the resolution gain factor was 2.6 ($NA_2 = 0.164$) and all four vertical bar patterns were clearly resolved in the reconstructed image, consistent with the enhanced horizontal cutoff frequency of 259 lp/mm. Upon careful inspection of Fig. 6(f), we discovered the horizontal bar patterns appeared to become somewhat vertical, albeit rather blurry. This effect is an artifact of coherent imaging with a passband that has been elongated in one dimension, namely the horizontal axis, as shown in Fig. 6(e). Edge ringing consequently occurs with a higher frequency in the

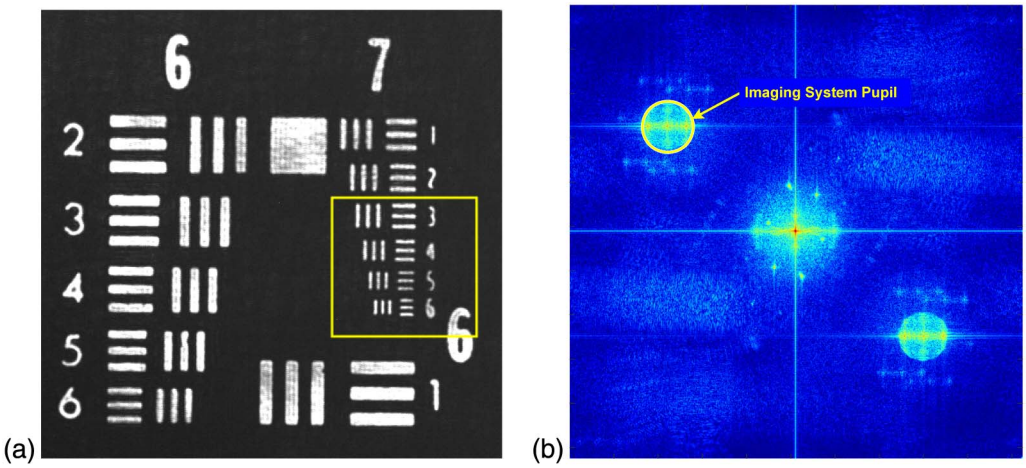

Fig. 5. (a) High-resolution coherent image of the USAF test target object used in the pupil multiplexing setup, obtained by opening the pupil in Fig. 4 to an NA of 0.18. The region-of-interest for subsequent testing (with the pupil stopped down to an NA of 0.063) is shown by the inset box (Group 7, Elements 3-6), corresponding to the smallest set of features available on the target. (b) Spectral magnitude of a typical pupil-multiplexed image hologram plotted on a log scale spanning four orders of magnitude.

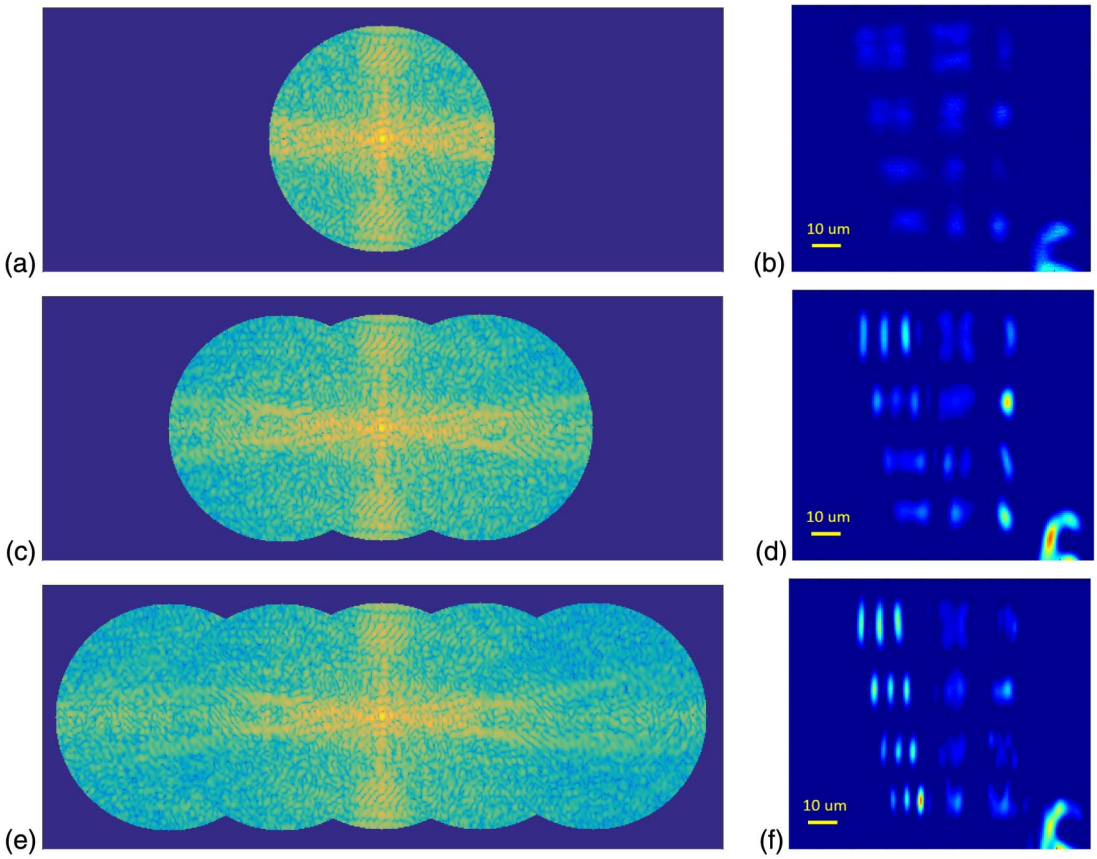

Fig. 6. Experimental results for the pupil multiplexing setup shown in Fig. 4 that demonstrate resolution enhancement in the horizontal direction. The images displayed in the right-hand column correspond to the inset box area of the test target as shown above in Fig. 5(a). (a) Image spectrum for the conventional system (no enhancement) with $NA_0 = 0.063$, and (b) the corresponding conventional image with none of the bar patterns being resolved. (c) Enhanced image spectrum found using three diffracted beams (0 and ± 1 orders) yielding $NA_1 = 0.114$, and (d) the corresponding image with the two upper sets of vertical bars now resolved. (e) Enhanced image spectrum found using five diffracted beams (0, ± 1 and ± 2 orders) yielding $NA_2 = 0.164$, and (f) the corresponding image with all four sets of vertical bars now resolved. The spectra are displayed on a log-magnitude scale spanning six orders of magnitude. The images, plotted on a linear scale, are found by inverse Fourier transforming the spectra after zero padding.

horizontal direction than in the vertical direction, thereby creating a vertical banding artifact.

B. Sequential Oblique Illumination

To test the sequential oblique illumination method, we used a demonstration system that implemented a version of the approach shown in Fig. 2. Instead of fabricating a custom tiled grating, we used a simple inexpensive holographic diffraction grating having a frequency of 500 lines/mm (Edmund Optics 54-510). We expanded the He–Ne laser beam to a diameter of approximately 30 mm, which illuminated a 2-mm diameter circular aperture mounted on an xy translation stage. We placed the grating 15.0 mm in front of the object. Figure 7 shows the illumination portion of the layout. The objective lens was a molded asphere with a focal length of 8.0 mm (Thorlabs A240), and the tube lens was the same 200-mm focal length plano-convex lens used in the pupil multiplexing system (Thorlabs LA1708), yielding an imaging path with a 25X magnification. The working distance from the object plane to the objective lens was 5.8 mm. The nominal imaging system had $NA_0 = 0.42$, as determined by a circular aperture stop of 3.4 mm diameter placed in the back focal plane of the objective.

We changed the object illumination angle by translating the 2-mm aperture in front of the grating, thereby shifting the various diffraction orders across the object. When the 2-mm aperture is centered on the optical axis, the illumination is normally incident (0-order beam); the ± 1 and ± 2 diffraction

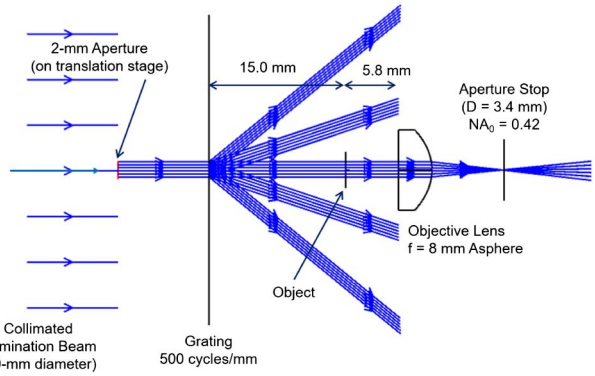

Fig. 7. Sequential oblique illumination experimental demonstration setup.

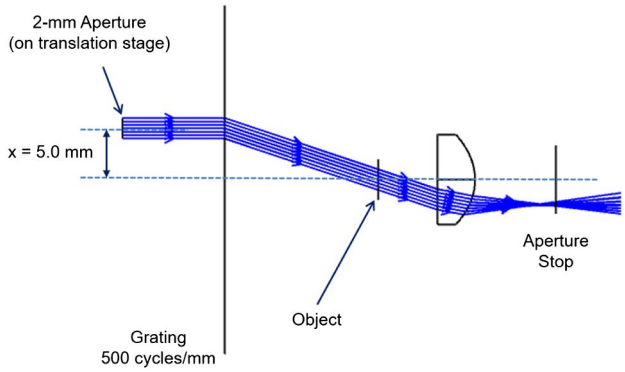

Fig. 8. Off-axis illumination using the −1 diffraction order of the grating. Shifting the aperture allows the other diffraction orders to provide illumination.

orders completely miss the objective lens aperture. This scheme is rather lossy, but is straightforward to implement.

We initially oriented the grating vector along the x-axis, so that shifting the aperture by 5.0 mm in the x-direction allowed the −1 diffraction order to illuminate the object at an angle of 18.5 degrees (NA = 0.32), as illustrated in Fig. 8. This beam appeared as a peak in the pupil at about 76% of cutoff. Shifting the aperture to $x = 12.25$ mm positioned the −2 diffraction order on the object with an illumination angle of 39.3 degrees (NA = 0.63, which falls outside the pupil). We also used similar shifts in the negative x-direction. We then rotated the grating by 90 degrees to align with the y-axis, and repeated the process. We recorded an image hologram for each illumination angle, yielding nine separate exposures.

The object was a test target comprising a pattern of concentric squares having a spatial frequency of 1,000 lines/mm, as shown in Fig. 9(a). Figure 9(b) shows the conventional intensity image of this test target. The horizontal and vertical line patterns, which are beyond the nominal coherent imaging system cutoff frequency of 664 cycles/mm ($NA_0 = 0.42$ at $\lambda = 633$ nm), are clearly not resolved. To direct the missing test pattern spectral content through the pupil, off-axis illumination in both the x- and y-directions, provided by grating diffraction as described above, is needed. When this is done, and the various spectral islands are combined using the approach outlined in Section 4, the resulting synthetic aperture spectrum can be reconstructed from the nine illumination angles, as shown in the log-magnitude plot of Fig. 9(c). As a consequence, the square test pattern becomes visible in the super-resolved image shown in Fig. 9(d). In this demonstration, the cutoff frequency along the x and y axes is extended to

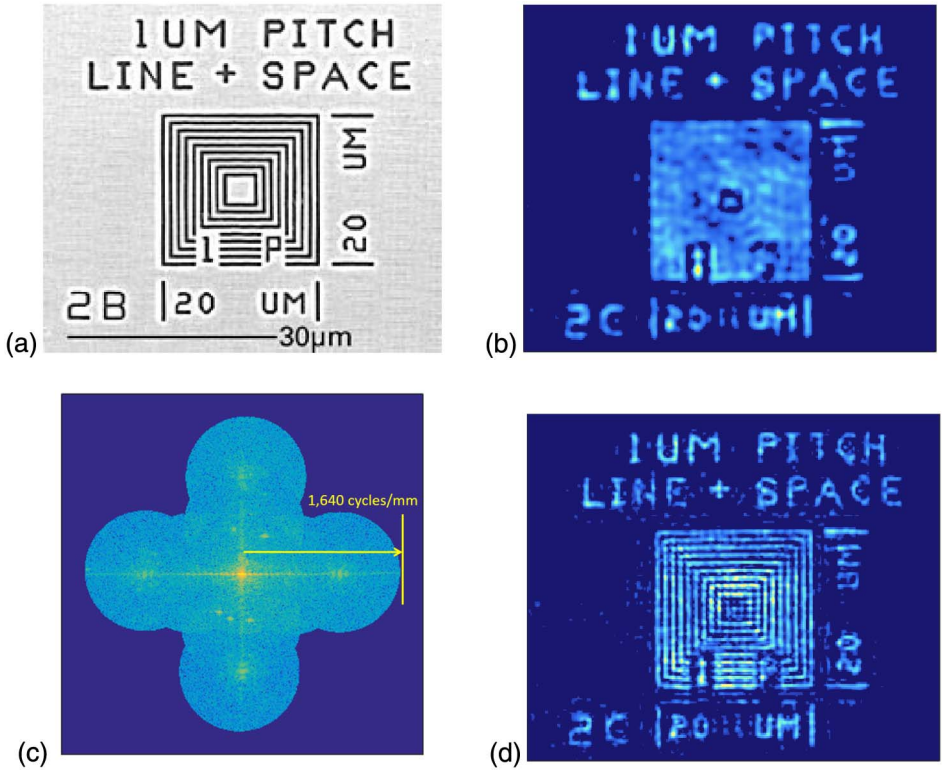

Fig. 9. (a) Test target object having a 1000 lp/mm square pattern, used to assess coherent superresolution imaging via the sequential oblique illumination method. (b) Experimental image of the target formed by conventional coherent imaging with $NA_0 = 0.42$, corresponding to a cutoff frequency of 664 cycles/mm (at 633 nm). The test pattern is clearly not resolved. (c) Experimentally reconstructed image spectrum magnitude (log scale) using nine exposures corresponding to the 0-order beam combined with the ±1 and ±2 orders along the x- and y-axis. The grating was first oriented along the x-axis, then rotated by ninety degrees to align with the y-axis. (d) Experimental superresolution image of the target formed by an inverse Fourier transform of the spectrum shown in (c) after zero padding to obtain spatial sampling equivalent to the camera pixel dimensions. The new cutoff frequency (along the x and y directions) is approximately 1640 cycles/mm, and the test pattern with a frequency of 1000 lp/mm is now resolved.

approximately 1,640 cycles/mm, providing a resolution gain factor of 2.5.

6. CONCLUSION

We have presented two methods to extend the resolution of a coherent optical imaging system. Both methods incorporate a diffraction grating to route high-frequency information that would otherwise be lost through the imaging system pupil. Digital holographic detection provides the optical field amplitude in the image plane. In one case, we placed the grating in near contact with the object (or it could be imaged onto the object) and it was moved over one grating period in equal-increment steps. Spectral aliasing was present, but linear signal processing, similar to that used in incoherent structured illumination, allowed us to recover the spectral islands. In the second case, we placed the grating some distance in front of the object, and a collimated input beam was translated sequentially across the grating to specific locations, thereby illuminating the object with a set of off-axis diffracted beams. For demonstration purposes we used a small aperture that was translated across a large diameter collimated beam; however, more efficient beam translating schemes are possible [21]. The various spectral islands were then directly measured without aliasing. We have discussed the details associated with stitching the spectral islands together to form a larger synthetic aperture.

Our experiments compared two techniques: pupil multiplexing and sequential oblique illumination. For pupil multiplexing, the grating must be moved in increments that are less than or equal to the enhanced image resolution. This requirement is not a significant limitation since modern piezo stages offer nanometer resolution. Perhaps of more concern is the impact of the camera's dynamic range. With sequential oblique illumination, the camera gain can be adjusted when recording the weaker dark-field image holograms associated with higher-order illumination. For pupil multiplexing, however, the camera gain must be set to accommodate the full range of image intensity, so the SNR associated with the weaker spectral components of the image could suffer more degradation. Finally, we note that when applying the pupil multiplexing approach to a well-behaved optical path, the phases of the higher-order $\widetilde{\mathbf{P}}$ matrix elements can likely be estimated from the directly measured $n = 0, \pm 1$ elements, which avoids the use of the more computationally intensive spectral overlap technique. In contrast, the higher-order beams in the sequential illumination scheme may not have a known phase relationship to the $n = 0, \pm 1$ beams, so the spectral overlap technique becomes essential. Both schemes are most useful when the NA of the objective lens is small, and the goal is to increase the effective NA to something closer to unity while preserving the wider field of view associated with a lower NA.

Regarding possible modifications, digital phase-shifting holography could be used rather than an offset reference wave. This approach would allow more efficient use of camera pixels for a wider measured field of view (e.g., by using a lower magnification with the same camera sensor), but would also require more exposures by at least a factor of three. In addition, the methods described can in principle use phase retrieval algorithms for each detected image intensity to eliminate the need for holographic detection. Such an approach, known as Fourier ptychography, replaces holographic detection with simpler detection of the low-resolution image intensity distributions obtained for each of a sequence of illumination angles, and uses iterative computational techniques to obtain a high-resolution image [29].

In summary, grating-based techniques are useful to generate a set of off-axis illumination beams over a wide range of incident angles. These beams are linearly separated in spatial frequency with a high degree of precision, which makes them well suited for implementation of coherent superresolution imaging. Other approaches that involve high-NA lenses in the illumination path are certainly possible, but it may be more prudent to simply use such lenses in the imaging path without adding the complexity of superresolution. However, if the goal is to construct an entire system using low-cost, low-NA lenses along with other simple optical elements, then the methods described here offer good options. More specifically, it is possible to image non-fluorescent objects with a large working distance and wide field of view, while employing grating-based superresolution to better observe the fine structure in the images.

REFERENCES

1. J. W. Goodman, *Introduction to Fourier Optics*, 3rd ed. (Roberts & Company, 2005).
2. J. Mertz, *Introduction to Optical Microscopy* (Roberts & Company, 2009).
3. S. Gazit, A. Szameit, Y. C. Eldar, and M. Segev, "Super-resolution and reconstruction of sparse sub-wavelength images," Opt. Express **17**, 23920–23946 (2009).
4. A. W. Lohmann and D. P. Paris, "Superresolution for nonbirefringent objects," Appl. Opt. **3**, 1037–1043 (1964).
5. A. W. Lohmann, R. G. Dorsch, D. Mendlovic, C. Ferreira, and Z. Zalevsky, "Space-bandwidth product of optical signals and systems," J. Opt. Soc. Am. A **13**, 470–473 (1996).
6. Z. Zalevsky, D. Mendlovic, and A. W. Lohmann, "Understanding superresolution in Wigner space," J. Opt. Soc. Am. A **17**, 2422–2430 (2000).
7. W. Lukosz, "Optical systems with resolving powers exceeding the classical limit," J. Opt. Soc. Am. **56**, 1463–1471 (1966).
8. A. Ilovitsh, V. Mico, and Z. Zalevsky, "Super resolved optical system for objects with finite sizes using circular gratings," Opt. Express **23**, 23667–23679 (2015).
9. J. García, V. Micó, D. Cojoc, and Z. Zalevsky, "Full field of view super-resolution imaging based on two static gratings and white light illumination," Appl. Opt. **47**, 3080–3087 (2008).
10. W. Lukosz, "Optical systems with resolving powers exceeding the classical limit. II," J. Opt. Soc. Am. **57**, 932–941 (1967).
11. D. Mendlovic, I. Kiryuschev, Z. Zalevsky, A. W. Lohmann, and D. Farkas, "Two-dimensional superresolution optical system for temporally restricted objects," Appl. Opt. **36**, 6687–6691 (1997).
12. M. G. L. Gustafsson, "Nonlinear structured-illumination microscopy: Wide-field fluorescence imaging with theoretically unlimited esolution," Proc. Natl. Acad. Sci. USA **102**, 13081–13086 (2005).
13. A. Faridian, D. Hopp, G. Pedrini, U. Eigenthaler, M. Hirscher, and W. Osten, "Nanoscale imaging using deep ultraviolet digital holographic microscopy," Opt. Express **18**, 14159–14164 (2010).
14. V. Mico, Z. Zalevsky, P. García-Martínez, and J. García, "Superresolved imaging in digital holography by superposition of tilted wavefronts," Appl. Opt. **45**, 822–828 (2006).
15. C. J. Schwarz, Y. Kuznetsova, and S. R. J. Brueck, "Imaging interferometric microscopy," Opt. Lett. **28**, 1424–1426 (2003).
16. A. Neumann, Y. Kuznetsova, and S. R. J. Brueck, "Structured illumination for the extension of imaging interferometric microscopy," Opt. Express **16**, 6785–6793 (2008).

17. J. H. Massig, "Digital off-axis holography with a synthetic aperture," Opt. Lett. **27**, 2179–2181 (2002).
18. C. Liu, Z. Liu, F. Bo, Y. Wang, and J. Zhu, "Super-resolution digital holographic imaging method," Appl. Phys. Lett. **81**, 3143–3145 (2002).
19. M. Paturzo, F. Merola, S. Grilli, S. D. Nicola, A. Finizio, and P. Ferraro, "Super-resolution in digital holography by a two-dimensional dynamic phase grating," Opt. Express **16**, 17107–17118 (2008).
20. T. R. Hillman, T. Gutzler, S. A. Alexandrov, and D. D. Sampson, "High-resolution, wide-field object reconstruction with synthetic aperture Fourier holographic optical microscopy," Opt. Express **17**, 7873–7892 (2009).
21. J. P. Wilde, Y. C. Eldar, and J. W. Goodman, "Grating-enhanced optical imaging," US Patent 8,841,591 (23 September 2014).
22. J. P. Wilde, J. W. Goodman, Y. C. Eldar, and Y. Takashima, "Grating-enhanced coherent imaging," in *Optics in the Life Sciences* (Optical Society of America, 2011).
23. J. P. Wilde, J. W. Goodman, Y. C. Eldar, and Y. Takashima, "Grating-enhanced coherent imaging," in *9th International Conference on Sampling Theory and Applications (SampTA)* (2011), p. P0213.
24. M. Mishali and Y. C. Eldar, "From theory to practice: Sub-Nyquist sampling of sparse wideband analog signals," IEEE J. Sel. Top. Signal Process. **4**, 375–391 (2010).
25. M. Mishali, Y. C. Eldar, O. Dounaevsky, and E. Shoshan, "Xampling: analog to digital at sub-Nyquist rates," IET Circuits Dev. Syst. **5**, 8–20 (2011).
26. Y. C. Eldar, *Sampling Theory: Beyond Bandlimited Systems* (Cambridge University, 2015).
27. S. A. Shroff, J. R. Fienup, and D. R. Williams, "OTF compensation in structured illumination superresolution images," Proc. SPIE **7094**, 709402 (2008).
28. S. A. Shroff, J. R. Fienup, and D. R. Williams, "Phase-shift estimation in sinusoidally illuminated images for lateral superresolution," J. Opt. Soc. Am. A **26**, 413–424 (2009).
29. G. Zheng, R. Horstmeyer, and C. Yang, "Wide-field, high-resolution Fourier ptychographic microscopy," Nat. Photonics **7**, 739–745 (2013).